Marine Structures 47 (2016) 23–41

Contents lists available at ScienceDirect

Marine Structures

journal homepage: www.elsevier.com/locate/marstruc

Analytical gradient-based optimization of offshore wind turbine substructures under fatigue and extreme loads

Kok-Hon Chew [a, b, *], Kang Tai [a], E.Y.K. Ng [a], Michael Muskulus [b]

[a] School of Mechanical and Aerospace Engineering, Nanyang Technological University, 639798, Singapore
[b] Department of Civil and Transport Engineering, Norwegian University of Science and Technology, 7491 Trondheim, Norway

ARTICLE INFO

Article history:
Received 1 September 2015
Received in revised form 30 December 2015
Accepted 21 March 2016

Keywords:
Offshore wind
Support structures
Optimization
Sensitivity analysis
Extreme load
Fatigue load

ABSTRACT

Design optimization of offshore wind turbine support structures is an expensive task due to the highly-constrained, non-convex and non-linear nature of the design problem. A good depth of detail in the problem formulation can give useful insights in the practical design process, but may also compromise the efficiency. This paper presents an analytical gradient-based method to solve the problem in an effective and efficient way. The design sensitivities of the objective and constraint functions are evaluated analytically, while the optimization procedure is performed in the time domain, subjected to sizing, eigenfrequency, extreme load and fatigue load constraints. A case study on the OC4 and UpWind jacket substructures show that the method was reliable and consistent in delivering superior efficiency and accuracy in the optimization study, as compared with the conventional finite difference approach. The global optimum was probably achieved in the design optimization process, where the large number of design constraints implemented can possibly be the blessing in disguise, as they seem to enable the optimizer to find the global optimum. Both the buckling and fatigue load constraints had significant influence over the design of tubular members and joints, while each component is oriented to maximize the utilization against the prescribed limit state functions.

1. Introduction

Offshore wind power has set foot in the renewable energy industry as early as 1991 when the Vindeby wind farm began operating in Danish waters. It was only over the last few years that the industry started to boom globally (mainly in Europe), when more focus is given to promote a clean and diverse energy mix, in view of the environmental impacts caused by fossil fuels [1]. Offshore wind is abundant and stable; and is a good power source to the populated cities mainly in coastal regions, without affecting the human habitat onshore. However, the current state of technology incurs a high levelized cost of energy (LCOE) which needs to be driven down [2]. For a 500-MW offshore wind farm to be built in the United States, recent studies have estimated that the capital costs are in the order of $5000/kW to $6000/kW, where the support structure system can contribute up to 22 percent of the total capital costs [3]. It has been identified as one of the key areas for cost reduction that can be attained through economies of scale and reduced material costs [4]. With the wind turbines growing larger and heavier, upscaling of current support structure designs to accommodate the increasing wind and wave dynamic loads when

* Corresponding author. 50 Nanyang Avenue, School of Mechanical and Aerospace Engineering, Nanyang Technological University, 639798, Singapore.
E-mail address: khc860113@gmail.com (K.-H. Chew).

http://dx.doi.org/10.1016/j.marstruc.2016.03.002
0951-8339/

venturing to deeper waters can be economically and technologically challenging. Development of novel concepts and evolution of existing designs are necessary to increase the structural strength-to-mass ratios for such applications, hence offering ample opportunity for structural optimization [5].

When optimizing the offshore wind turbine (OWT) support structures, accurate and extensive load simulations are required to develop reliable and cost-effective designs. On the one hand, coupled dynamic simulations are performed in the time domain, in order to capture the coupling effects and non-linearities within the aero-hydro-servo-elastic analysis [6]. On the other hand, the simulations have to be repeated for multiple design load cases (DLCs) representing different operational and environmental conditions, in accordance with the international standards [7]. Specialized software that supports the aero-hydro-servo-elastic modeling and analysis is normally employed to carry out the simulations. Nevertheless, static load analysis is still commonly employed within the industry, especially the optimization design studies. For instance, Uys et al. [8] minimized the material and manufacturing costs of a ring-stiffened monopile tower subjected to various buckling constraints, by using static wind loads. As for the dynamic response optimization, transient loads introduce time-dependent constraints, which can be treated in a discretized time domain by various approaches reviewed in [9]. Besides, design optimization of offshore tripod structures subjected to extreme loading conditions using the reliability-based and robust design optimization was investigated by Karadeniz et al. [10] and Yang and Zhu [11], respectively, while considering uncertainties in geometry, material properties and load parameters.

So far the aforementioned studies did not include fatigue failure analysis in the design process, which is rather critical for offshore structures. OWT support structures experience vibrations due to the excitation arising from environmental loads and rotor rotations. The fatigue load constraints are sensitive to dynamic response histories, and the evaluations of gradient information using the efficient analytical methods are very challenging [12]. Various simulation-based optimization approaches can be employed to combine both fatigue and extreme load constraints. Chew et al. [13] compared 3-legged and 4-legged jacket substructures subjected to both constraints in the time domain by varying the diameter-to-thickness ratios. Long et al. [14] performed optimization on a full lattice tower using a sequential approach in the frequency domain, where a static design was obtained from the extreme load analysis followed by redesign of member thicknesses against the fatigue loads. Furthermore, heuristic methods were implemented to search for the global optimal solution. Yoshida [15] optimized the dimensions and the positions of flanges and access ports for a wind turbine tower using the genetic algorithm. Schafhirt et al. [16] improved the method by incorporating reanalysis within the genetic algorithm to speed up the optimization process while reducing the number of iterations.

In general, the design optimization procedure requires a large number of iterative calculations since the problem is highly constrained and non-convex. Gradient-based optimization is well-known for fast convergence by utilizing sensitivity information to determine the best direction for improvement, but has the problem of getting stuck in local optima. Currently, most of the research conducted has adopted finite difference methods to obtain the gradients of objective and constraint functions, due to the complexity of problem formulations and the high dependency on specialized software to solve the dynamic problems [17,18]. Recent studies have shown that the finite difference approximation can be erroneous when used in the evaluation of gradients for extreme and fatigue load constraints during the design of OWT structures [19,20]. This may result in an inefficient and unreliable gradient-based optimization procedure.

In this paper, an integrated optimization framework that is based on the analytical gradient-based approach is proposed for the design of OWT support structures. The purpose of the study is:

1. To investigate the overall performance of the proposed methodology, by evaluating (i) the accuracy of the dynamic modeling and analysis; (ii) the efficiency of the analytical optimization approach and (iii) whether the method can find or get close to the global optimum, or will get stuck in a local optimum.
2. To study the influence of various design constraints (eigenfrequency, extreme load and fatigue load constraints) on the structural design and the optimization procedure.

Section 2 provides the problem formulation and discusses various design constraints implemented in the study. Section 3 illustrates the optimization framework. Section 4 presents a case study, followed by results and discussion in Section 5.

2. Optimal design problem formulation

The dynamic response optimization of OWT support structures is a constrained non-linear programming (NLP) problem, which can be illustrated using the following expression:

$$\text{Find } \mathbf{b} \tag{1}$$

$$\text{to minimize } f(\mathbf{b}) \tag{2}$$

$$\text{subject to } g_i(\mathbf{b}, \mathbf{z}(t_j), t_j) \leq 0; \quad i = 1, \cdots, p, \quad j = 1, \cdots, q \tag{3}$$

$$\text{and } [\mathbf{M}(\mathbf{b})]\ddot{\mathbf{z}}(t_j) + [\mathbf{C}(\mathbf{b})]\dot{\mathbf{z}}(t_j) + [\mathbf{K}(\mathbf{b})]\mathbf{z}(t_j) - \mathbf{f}(\mathbf{b}, t_j) = 0 \tag{4}$$

where f is the objective function; g_i is the constraint function; $\mathbf{b}$ is the design variable vector; $\mathbf{z}(t_j)$, $\dot{\mathbf{z}}(t_j)$ and $\ddot{\mathbf{z}}(t_j)$ are the displacement, velocity and acceleration vectors; t_j is the jth time step; $[\mathbf{M}(\mathbf{b})]$, $[\mathbf{C}(\mathbf{b})]$ and $[\mathbf{K}(\mathbf{b})]$ are the system mass, damping and stiffness matrices, respectively; and $\mathbf{f}(\mathbf{b}, t_j)$ is the force vector.

2.1. Objective function

In general, the support structure can be modeled as an assemblage of beam elements, connected through nodes in resemblance to the actual structures, e.g. monopile, spaceframe and tripod structures. The objective function to be minimized is the structural mass and is given by

$$f = \sum_{n=1}^{N} \rho_s A_n(\mathbf{b}) L_n \tag{5}$$

where ρ_s is the material density [kg/m^3]; and $A_n(\mathbf{b})$ and L_n are the cross-sectional area [m^2] and length [m] of the nth member. This is a simplified representation of the cost function since other cost components that are incurred in the design life cycle of OWT support structures, such as manufacturing, installation and maintenance costs are excluded. For tubular structures, $A_n(\mathbf{b}) = \pi(D_n T_n - T_n^2)$ and $\mathbf{b} = [D_1, T_1, D_2, T_2, \ldots, D_{M/2}, T_{M/2}]$, where D_n and T_n are the diameter [m] and thickness [m] of nth member; and M is the total number of design variables.

2.2. Design constraints

The design constraints implemented in the study include various limit state functions as prescribed by the design standards and recommended practices used within the offshore and wind industries [7,21,22]. They are based upon the load and resistance factor design (LRFD) method, and can be classified into sizing, eigenfrequency, extreme load and fatigue load constraints.

2.2.1. Sizing constraints

Sizing constraints define the lower and upper bounds of design variables $\mathbf{b}$ as well as the geometrical relationships among the variables, e.g. D_n/T_n, etc. They can be expressed as

$$g_1 = \mathbf{b}_{min} \leq \mathbf{b} \leq \mathbf{b}_{max} \tag{6}$$

$$g_2 = [\mathbf{A}_{ineq}]\mathbf{b} - \mathbf{c}_{ineq} \leq 0 \tag{7}$$

where $\mathbf{b}_{min}$ is the lower bound and $\mathbf{b}_{max}$ is the upper bounds of $\mathbf{b}$; $[\mathbf{A}_{ineq}]$ and $\mathbf{c}_{ineq}$ are the linear inequality matrix and vector. The matrix $[\mathbf{A}_{ineq}]$ and vector $\mathbf{c}_{ineq}$ can be established from the validity range of $\mathbf{b}$ provided for the prescribed limit state functions (see subsection 4.1).

2.2.2. Eigenfrequency constraints

The natural frequencies of the overall OWT system have to be assessed against the excitation frequency zones caused by environmental loads (e.g. winds and waves) and rotor rotations, so as to avoid (or minimize) the risk of resonance. In modern variable speed turbines, the main rotor excitation frequencies exist as 1P and nP frequency bands, where 1P is associated with the rotor rotational revolutions per minute (RPM) while nP is due to the blade passing frequency, i.e. nth multiple of the rotor rotational RPM where n is the number of blades. Hence for a three-bladed rotor, the first mode eigenfrequencies f_1 are usually designed to lie in the soft-stiff region as bounded between $1\mathbf{P_U}$ and $3\mathrm{P_L}$, i.e.

$$g_3 = 1\mathrm{P_U} \leq f_1 \leq 3\mathrm{P_L} \tag{8}$$

where $1\mathrm{P_U}$ is the upper bound of 1P range [Hz] and $3\mathrm{P_L}$ is the lower bound of 3P range [Hz]. This is a more economical approach to design a bottom-fixed support structure that withstands the excitation through structural resistance [23].

2.2.3. Extreme load constraints

The ultimate limit state (ULS) analysis of support structures is performed to check if structural strength and stability requirements are fulfilled in the design process when subjected to extreme loading conditions, which includes yield checks on beams and joints as well as the buckling assessments. In this study, the extreme load constraints are formed in accordance with the limit state functions specified in the NORSOK N-004 [22]. Under the complicated environmental conditions, the offshore tubular members are potentially exposed to any combination of axial tension, axial compression, bending, shear and

hydrostatic loads. The hydrostatic pressure also generates an additional axial compressive force if the ends are capped. The limit state functions for tubular members under combined loads are given by

- Combined axial tension and bending:

$$g_4 = \left(\frac{N_{t,Sd}}{N_{t,Rd}}\right)^{1.75} + \frac{\sqrt{M_{y,Sd}^2 + M_{z,Sd}^2}}{M_{Rd}} - 1.0 \le 0 \tag{9a}$$

$$g_4 = \frac{\sigma_{at,Sd}}{f_{th,Rd}} + \frac{\sqrt{\sigma_{my,Sd}^2 + \sigma_{mz,Sd}^2}}{f_{mh,Rd}} - 1.0 \le 0 \tag{9b}$$

- Combined axial compression and bending, where column buckling is studied in Eqs. (10a) and (10b):

$$g_5 = \frac{N_{c,Sd}}{N_{c,Rd}} + \frac{1}{M_{Rd}}\left[\left(\frac{C_{my}M_{y,Sd}}{1-\frac{N_{c,Sd}}{N_{Ey}}}\right)^2 + \left(\frac{C_{mz}M_{z,Sd}}{1-\frac{N_{c,Sd}}{N_{Ez}}}\right)^2\right]^{0.5} - 1.0 \le 0 \tag{10a}$$

$$g_5 = \frac{\sigma_{ac,Sd} - \sigma_{q,Sd}}{f_{ch,Rd}} + \frac{1}{f_{mh,Rd}}\left[\left(\frac{C_{my}\sigma_{my,Sd}}{1-\frac{\sigma_{ac,Sd}-\sigma_{q,Sd}}{f_{Ey}}}\right)^2 + \left(\frac{C_{mz}\sigma_{mz,Sd}}{1-\frac{\sigma_{ac,Sd}-\sigma_{q,Sd}}{f_{Ez}}}\right)^2\right]^{0.5} - 1.0 \le 0 \tag{10b}$$

$$g_6 = \frac{N_{c,Sd}}{N_{cl,Rd}} + \frac{\sqrt{M_{y,Sd}^2 + M_{z,Sd}^2}}{M_{Rd}} - 1.0 \le 0 \tag{11a}$$

$$g_6 = \frac{\sigma_{ac,Sd}}{f_{cl,Rd}} + \frac{\sqrt{\sigma_{my,Sd}^2 + \sigma_{mz,Sd}^2}}{f_{mh,Rd}} - 1.0 \le 0 \tag{11b}$$

$$g_7 = \frac{\sigma_{c,Sd} - 0.5\frac{f_{he}}{\gamma_m}}{\frac{f_{cle}}{\gamma_m} - 0.5\frac{f_{he}}{\gamma_m}} + \left(\frac{\sigma_{p,Sd}}{\frac{f_{he}}{\gamma_m}}\right)^2 - 1.0 \le 0 \tag{12}$$

- Interaction shear, bending moment and torsional moment:

$$g_8 = \begin{cases} \dfrac{M_{Sd}}{M_{Red,Rd}} - \sqrt{1.4 - \dfrac{V_{Sd}}{V_{Rd}}} \le 0 & \text{for } \dfrac{V_{Sd}}{V_{Rd}} \ge 0.4 \\ \dfrac{M_{Sd}}{M_{Red,Rd}} - 1.0 \le 0 & \text{for } \dfrac{V_{Sd}}{V_{Rd}} < 0.4 \end{cases} \tag{13}$$

- Hoop buckling:

$$g_9 = \frac{\sigma_{p,Sd}}{f_{h,Rd}} - 1.0 \leq 0 \tag{14}$$

where $N_{t,Sd}(\sigma_{at,Sd})$, $N_{c,Sd}(\sigma_{ac,Sd})$, $M_{y,Sd}(\sigma_{my,Sd})$, $M_{z,Sd}(\sigma_{mz,Sd})$, V_{Sd} are the design axial tensile force [N], compressive force [N], bending moments [N m] about member y-axis (in-plane) and z-axis (out-of-plane) and shear force [N], respectively; $N_{t,Rd}(f_{th,Rd})$, $N_{c,Rd}(f_{ch,Rd})$, $N_{cl,Rd}(f_{cl,Rd})$, $N_{Ey}(f_{Ey})$, $N_{Ez}(f_{Ez})$, $M_{Rd}(f_{mh,Rd})$ and V_{Rd} are the design resistance for axial tension [N], axial compression [N], local buckling [N], Euler buckling (member y- and z- axes) [N], bending [Nm] and shear [N], respectively; $\sigma_{p,Sd}$, $\sigma_{q,Sd}$ and $\sigma_{c,Sd}$ are the design hoop stress, capped-end compressive stress and maximum combined compressive stress, respectively; and $f_{h,Rd}$, f_{he}, f_{cle}, C_{my}, C_{mz} and γ_m are the design hoop buckling strength, elastic hoop buckling strength, characteristic elastic local buckling strength, reduction factors (member y- and z-axes) and partial safety factor for material, respectively. The symbols in parentheses refer to the corresponding stress terms that account for the external hydrostatic pressure effects. All stress units are in Pa. Eqs. (9a), (10a) and (11a) and (13) are applicable to the members which are free of hydrostatic pressure, such as, beams above the mean sea level (MSL) or flooded internally, whereas Eqs. (9b), (10b), (11b), (12) and (14) are pertinent to the submerged members which experience hydrostatic pressure externally.

Similarly, the resistance of tubular joints N_{Rdj}, $M_{y,Rdj}$ and $M_{z,Rdj}$ is checked to conform to the interaction equation for combined axial force and bending moments in the braces:

$$g_{10} = \frac{N_{Sd}}{N_{Rdj}} + \left(\frac{M_{y,Sd}}{M_{y,Rdj}}\right)^2 + \frac{M_{z,Sd}}{M_{z,Rdj}} - 1.0 \leq 0. \tag{15}$$

The characteristic resistance depends on the strength factor Q_u and the chord action factor Q_f, which vary with respect to the joint configuration (i.e. joint type and joint dimension), material strength, as well as the presence of factored actions within the chords. Since the extreme load constraints are time-dependent, they are supposed to be satisfied at all time steps. Several methods are available to handle this type of constraint, and the worst case approach was implemented in this study. The method identifies the maximum violated limit state values in time as design constraints; while gradients are calculated for the constraints active at those time points.

2.2.4. Fatigue load constraints

Fatigue failure often occurs around the weld toes at member connections due to high stress concentration in long term cyclic loads. It is another important aspect to be analyzed when designing offshore structures. This failure mode is cumulative along the response histories. Often the fatigue damage is calculated on the response data available for a certain simulation period, followed by a projection to the entire design lifespan (typically 20 years or more). One way to perform the fatigue limit state (FLS) analysis is by using the S-N curve approach. According to the DNV Recommended Practice, eight hot spot stresses (HSSs) around the circumferential of an intersection are determined from superposition of nominal axial and bending stresses that are pre-multiplied by stress concentration factors (SCFs) [24]. The SCFs can be calculated using empirical formulae (e.g. Eftymiou's formulae) which vary with respect to the joint configuration and action type. The S-N curves are based on fatigue test data collected from experiments performed at constant amplitude cyclic loads. As for HSSs which are variable in amplitude, a cycle counting method such as ASTM's rainflow counting algorithm has to be used to determine the effective stress ranges and the corresponding number of stress cycles [25]. The individual stress range is then compared against the S-N curves to calculate the fatigue damage ratio. By applying the Palmgren-Miner's rule, the damage is summed up linearly for each stress range which gives the total accumulated damage. The unity check of fatigue load constraint that accounts for the thickness effect is

$$g_{11} = \sum_{v=1}^{V}\left[P_v \sum_{u=1}^{U} \frac{1}{\bar{a}\eta}\left(\frac{T}{T_{ref}}\right)^{mk} n_u (\triangle\sigma_{u,HSS})^m\right] - 1 \leq 0 \tag{16}$$

where $\bar{a}$ is the intercept of the design S-N curve with log N axis; m is the negative inverse slope of the S-N curve; $\triangle\sigma_{u,HSS}$ is the uth HSS stress range [MPa]; n_u is the number of stress cycles in $\triangle\sigma_{u,HSS}$; U is the total number of stress ranges; η is the usage factor; T, T_{ref} and k are the member thickness [m], reference thickness [m] and thickness exponent, respectively; P_v is the probability of vth event; and V is total number of FLS events.

3. Integrated optimization methodology

An integrated code for dynamics analysis and structural optimization was developed in Matlab (Ver. 2014b, The Mathworks, Inc.) to solve the described optimal design problem. The process workflow is shown in Fig. 1.

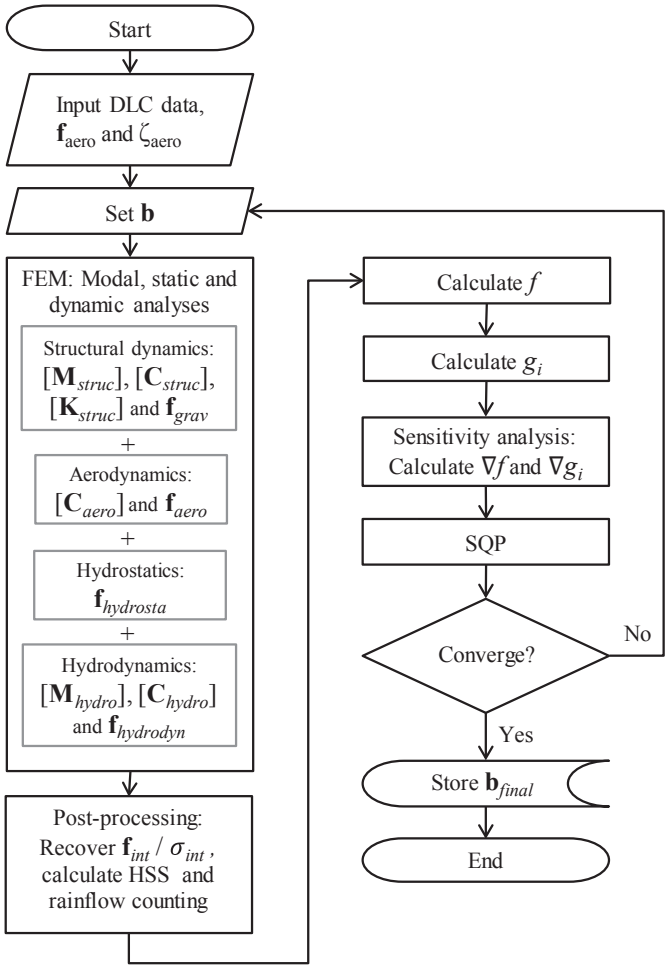

Fig. 1. Integrated optimization process proposed to solve the optimal design problem of OWT support structures.

3.1. Structural dynamics

The method assumes a linear hydro-elastic OWT system with the aero-servo effect implemented through a decoupled model. When solving the response dynamics, Eq. (4) can be broken down into the following static and dynamic problems:

$$[\mathbf{K}_{struc}]\mathbf{z}_{sta} - (\mathbf{f}_{grav} + \mathbf{f}_{hydrosta}) = 0 \tag{17}$$

$$\left(\left[\mathbf{M}_{hydro}\right] + [\mathbf{M}_{struc}]\right)\ddot{\mathbf{z}}_{dyn}(t_j) + \left([\mathbf{C}_{aero}] + \left[\mathbf{C}_{hydro}\right] + [\mathbf{C}_{struc}]\right)\dot{\mathbf{z}}_{dyn}(t_j) + [\mathbf{K}_{struc}]\mathbf{z}_{dyn}(t_j) - \left(\mathbf{f}_{aero}(t_j) + \mathbf{f}_{hydrodyn}(t_j)\right) = 0. \tag{18}$$

The basic structural model includes a rotor-nacelle assembly (RNA) and a support structure system; and is represented by three-dimensional beam elements (see Fig. 2(a)). Classical Euler-Bernoulli beam theory was used in the finite element method (FEM). The theory ignores shear deformation and rotational inertia effects and is suitable for long and slender beams. The mass matrix $[\mathbf{M}_{struc}]$ and stiffness matrix $[\mathbf{K}_{struc}]$ were calculated for the overall structural model, while Rayleigh damping was incorporated as the structural damping $[\mathbf{C}_{struc}]$. The inclusion of a full RNA in the OWT modeling enables a more accurate estimation of the system eigenmodes, as compared to using an equivalent lumped mass model for the RNA. Moreover, additional mass effects arising from the hydrodynamic added mass, water in flooded legs and marine growth were captured as $[\mathbf{M}_{hydro}]$ in the modal analysis. The gravitational forces $\mathbf{f}_{grav}$ were calculated for all structural elements and marine growth. The Newmark-beta integration method was used to solve Eq. (18) to obtain the dynamic response $\mathbf{z}_{dyn}(t_j)$. After adding the static response $\mathbf{z}_{sta}$ in Eq. (17), internal forces $\mathbf{f}_{int}$ and stresses σ_{int} can be recovered using

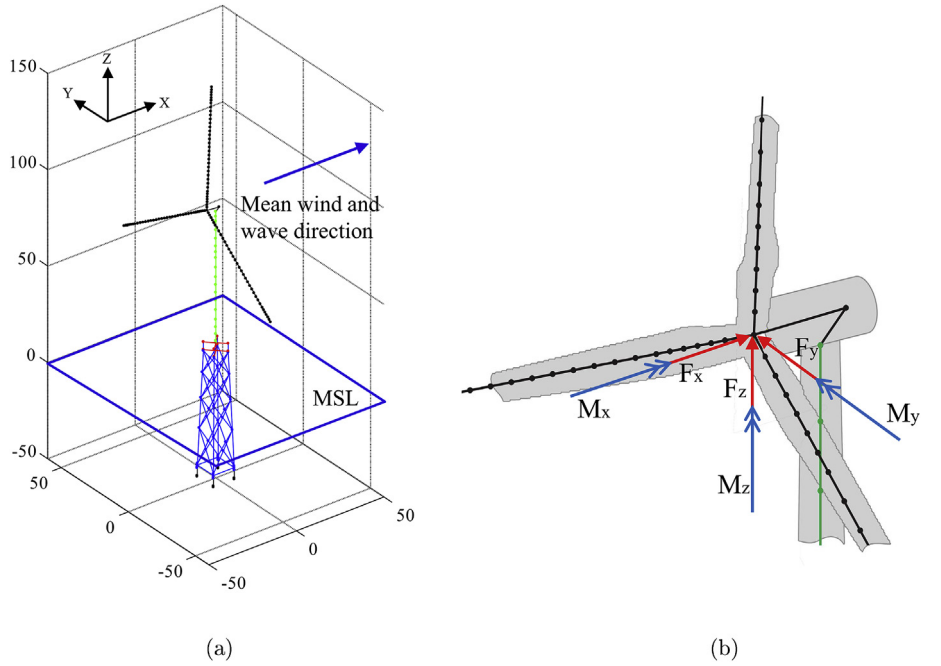

Fig. 2. (a) Finite element model of OWT system and (b) decoupled aerodynamic loads on RNA.

$$\mathbf{f}_{int} = [\mathbf{D}][\mathbf{B}]\mathbf{z}_{local} \tag{19}$$

where $\mathbf{f}_{int}$ is the internal force vector; [**D**] is the constitutive matrix, formed by EA, EI_y and EI_z; [**B**] is the strain-displacement matrix; and $\mathbf{z}_{local}$ is the total nodal displacement vector in local coordinates.

3.2. Aerodynamic loads

The decoupled aero-servo load was calculated externally using FEDEM Windpower Version R7.1.1 developed by FEDEM Technology AS, through a co-simulation with AeroDyn and TurbSim by National Renewable Energy Laboratory (NREL). FEDEM Windpower is an integrated multibody-FEM solver that supports control modeling [26]. Aerodyn calculates the aerodynamic forces using either the full Blade Element Momentum (BEM) or the Generalized Dynamic Wake (GDW) methods that account for tip or hub loss corrections [27]. TurbSim is the pre-processing tool used to generate the turbulent wind input files [28]. Simulations under various wind states as specified in the DLCs were performed on a numerical wind turbine model which was fixed at the yaw node. After subtracting the baseline results modeled in a still wind condition, forces and moments in six degrees of freedom (DOF) experienced at the hub node were extracted and imported into the in-house FEM model as the aerodynamic force vector $\mathbf{f}_{aero}(t_j)$ (see Fig. 2(b)). In addition, the linear aerodynamic damping ratios ζ_{aero} were estimated for each wind speed bin within the DLC, by analyzing the free decay vibration of the tower top motion upon exerting a pulse load on the turbine simulated under the turbulent wind fields, as described in Ref. [29]. The aerodynamic damping matrix [$\mathbf{C}_{aero}$] was formed by calculating the aerodynamic damping coefficient c_{aero} for the fore-aft motion based on

$$c_{aero} = \frac{2\zeta_{aero}K_{modal}}{\omega_1} \tag{20}$$

where K_{modal} is the modal spring constant [N/m] and ω_1 is the first mode fore-aft eigen frequency [rad/s]. The K_{modal} can be determined using $F/u(\mathbf{b})$, when applying an arbitrary horizontal force within the elastic limit F onto the hub node and obtaining the corresponding horizontal deflection $u(\mathbf{b})$ from the FEM code.

3.3. Hydrostatic and hydrodynamic loads

The submerged parts of the substructure experience a hydrostatic force $\mathbf{f}_{hydrosta}$ and a hydrodynamic force $\mathbf{f}_{hydrodyn}(t_j)$. The $\mathbf{f}_{hydrosta}$ or buoyancy was computed as the weight of displaced liquid. In the case of flooded members, additional enclosed liquid mass has to be accounted for. Both buoyancy and internal mass were summed up to the MSL. Moreover, the code can

also model marine growth around the tubular members. Regarding the hydrodynamic force, it was calculated using the empirical Morison's formula:

$$\mathrm{d}\mathbf{f}_{Morison} = \left[C_m \frac{\pi \rho_w D^2}{4} \dot{\mathbf{v}}_w - C_a \frac{\pi \rho_w D^2}{4} \ddot{\mathbf{z}}\right] \mathrm{d}L + C_d \frac{\rho_w D}{2} (\mathbf{v}_w - \dot{\mathbf{z}}) \left|\mathbf{v}_w - \dot{\mathbf{z}}\right| \mathrm{d}L \tag{21}$$

where C_m, C_a and C_d are the inertial, added mass and drag coefficients, respectively. The theory neglects the gradients of fluid particle velocities and accelerations in normal directions upon passing through the members; and therefore is applicable only to slender structures which satisfy $\lambda/D > 5$, where λ is the wavelength and D is the diameter. It consists of an inertial component which depends on both the water particle acceleration $\dot{\mathbf{v}}_w(t_j)$ and the structural acceleration $\ddot{\mathbf{z}}(t_j)$, as well as a viscous drag term which is linearly proportional to the square of the relative velocity between the water particle $\mathbf{v}_w(t_j)$ and the structure $\dot{\mathbf{z}}(t_j)$. The quadratic drag force was expanded into $-[\mathbf{C}_{hydro}(\mathbf{v}_w)]\dot{\mathbf{z}} + \mathbf{f}_{drag}(\mathbf{v}_w)$ while assuming that $\dot{\mathbf{z}} \ll \mathbf{v}_w$, where $[\mathbf{C}_{hydro}]$ is the linearized hydrodynamic damping matrix and $\mathbf{f}_{drag}(\mathbf{v}_w)$ is the non-linear hydrodynamic drag force for fixed structures. Apart from the hydrodynamic added mass, i.e. second term in Eq. (21), and $[\mathbf{C}_{hydro}]$, the remaining terms formed the $\mathbf{f}_{hydrodyn}(t_j)$.

3.4. Sensitivity analysis

Design sensitivity analysis is a process that calculates the rate of change of a performance measure with respect to the design variables. The performance measures in this context refer to the objective and constraint functions. The rate of change or simply gradient is required by the optimizer to decide the best direction for improvement during the optimization process. In this study, the gradients were calculated using the direct differentiation method (DDM) as

$$\nabla f = \frac{\partial f}{\partial \mathbf{b}} \tag{22}$$

$$\nabla g_i = \frac{\partial g_i}{\partial \mathbf{b}} + \frac{\partial g_i}{\partial \mathbf{z}} \frac{\mathrm{d}\mathbf{z}}{\mathrm{d}\mathbf{b}} \tag{23}$$

where ∇f is the gradient of objective function and ∇g_i is the gradient of constraint function i [30].

The calculations of ∇f, ∇g_1 and ∇g_2 were straightforward. As for the extreme load constraints, ∇g_i could be treated in two parts. Firstly, the $\frac{\mathrm{d}\mathbf{z}}{\mathrm{d}\mathbf{b}}$ in Eq. (23) is the sum of derivatives for static and dynamic displacements, i.e.

$$\frac{\mathrm{d}\mathbf{z}}{\mathrm{d}\mathbf{b}} = \frac{\mathrm{d}\mathbf{z}_{sta}}{\mathrm{d}\mathbf{b}} + \frac{\mathrm{d}\mathbf{z}_{dyn}}{\mathrm{d}\mathbf{b}}. \tag{24}$$

Both derivatives were solved using

$$\frac{\mathrm{d}\mathbf{z}_{sta}}{\mathrm{d}\mathbf{b}} = [\mathbf{K}]^{-1} \left(\frac{\mathrm{d}\mathbf{f}_{sta}}{\mathrm{d}\mathbf{b}} - \frac{\mathrm{d}[\mathbf{K}]}{\mathrm{d}\mathbf{b}} \mathbf{z}_{sta}\right) \tag{25}$$

and

$$[\mathbf{M}] \frac{\mathrm{d}^2}{\mathrm{d}t^2} \left(\frac{\mathrm{d}\mathbf{z}_{dyn}}{\mathrm{d}\mathbf{b}}\right) + [\mathbf{C}] \frac{\mathrm{d}}{\mathrm{d}t} \left(\frac{\mathrm{d}\mathbf{z}_{dyn}}{\mathrm{d}\mathbf{b}}\right) + [\mathbf{K}] \left(\frac{\mathrm{d}\mathbf{z}_{dyn}}{\mathrm{d}\mathbf{b}}\right) = \frac{\mathrm{d}\mathbf{f}_{dyn}}{\mathrm{d}\mathbf{b}} - \frac{\mathrm{d}[\mathbf{M}]}{\mathrm{d}\mathbf{b}} \ddot{\mathbf{z}}_{dyn} - \frac{\mathrm{d}[\mathbf{C}]}{\mathrm{d}\mathbf{b}} \dot{\mathbf{z}}_{dyn} - \frac{\mathrm{d}[\mathbf{K}]}{\mathrm{d}\mathbf{b}} \mathbf{z}_{dyn}\ , \tag{26}$$

respectively. Eq. (26) is a second order differential equation obtained when differentiating Eq. (18) with respect to $\mathbf{b}$.

The matrices $\frac{\mathrm{d}[\mathbf{M}]}{\mathrm{d}\mathbf{b}}$, $\frac{\mathrm{d}[\mathbf{C}]}{\mathrm{d}\mathbf{b}}$ and $\frac{\mathrm{d}[\mathbf{K}]}{\mathrm{d}\mathbf{b}}$ are the derivatives of system matrices $[\mathbf{M}]$, $[\mathbf{C}]$ and $[\mathbf{K}]$ that include the aero-hydro-elastic contributions, as mentioned earlier. Meanwhile, $\frac{\mathrm{d}\mathbf{f}_{sta}}{\mathrm{d}\mathbf{b}}$ denotes the derivative of static forces, i.e. $\mathbf{f}_{hydrosta}$ and $\mathbf{f}_{grav}$, while $\frac{\mathrm{d}\mathbf{f}_{dyn}}{\mathrm{d}\mathbf{b}}$ refers to the derivative of dynamic forces, i.e. $\mathbf{f}_{hydrodyn}$. Note that the $\mathbf{f}_{aero}$ does not vary with $\mathbf{b}$ in the decoupled method.

Secondly, the design load (numerator terms) and design resistance (denominator terms) in the constraint functions $g_4 - g_{10}$ can be expressed as functions of internal forces and geometric variables. As a result, g_i are generally explicit functions of $\mathbf{b}$ and $\mathbf{z}$. The partial derivatives $\frac{\partial g_i}{\partial \mathbf{b}}$ and $\frac{\partial g_i}{\partial \mathbf{z}}$ in Eq. (23) could be evaluated readily.

With regards to the fatigue load constraint, the calculation of gradients was handled differently. The differentiation of Eq. (16) against $\mathbf{b}$ gives

$$\nabla g_{11} = \sum_{v=1}^{V} \left[P_v \sum_{u=1}^{U} \frac{mk}{\overline{a}\eta} \left(\frac{1}{T_{ref}}\right)^{mk} T^{mk-1} \frac{\mathrm{d}T}{\mathrm{d}\mathbf{b}} n_u \left(\triangle\sigma_{u,HSS}\right)^m\right] + \sum_{v=1}^{V} \left[P_v \sum_{u=1}^{U} \frac{m}{\overline{a}\eta} \left(\frac{T}{T_{ref}}\right)^{mk} n_u \left(\triangle\sigma_{u,HSS}\right)^{m-1} \frac{\mathrm{d}\triangle\sigma_{u,HSS}}{\mathrm{d}\mathbf{b}}\right]. \tag{27}$$

The $\triangle\sigma_{u,HSS}$ here refers to the individual stress range without binning into blocks, while the stress cycle n_u corresponds to either a half or full cycle for the $\triangle\sigma_{u,HSS}$. By doing so, the $\frac{dn_u}{d\mathbf{b}}$ term could be neglected in the formulation. Among the terms, the derivative of stress range $\frac{d\triangle\sigma_{u,HSS}}{d\mathbf{b}}$ was calculated by taking the difference of HSS sensitivities $\frac{d\sigma_{u,HSS}}{d\mathbf{b}}$ at $t_j = t_{u,1}$ and $t_j = t_{u,2}$:

$$\frac{d\triangle\sigma_{u,HSS}}{d\mathbf{b}} = \begin{cases} \frac{d\sigma_{u,HSS}(t_j)}{d\mathbf{b}}\Big|_{t_j=t_{u,1}} - \frac{d\sigma_{u,HSS}(t_j)}{d\mathbf{b}}\Big|_{t_j=t_{u,2}} & \text{for } \sigma_{u,HSS}(t_{u,1}) > \sigma_{u,HSS}(t_{u,2}) \\ \frac{d\sigma_{u,HSS}(t_j)}{d\mathbf{b}}\Big|_{t_j=t_{u,2}} - \frac{d\sigma_{u,HSS}(t_j)}{d\mathbf{b}}\Big|_{t_j=t_{u,1}} & \text{for } \sigma_{u,HSS}(t_{u,2}) > \sigma_{u,HSS}(t_{u,1}) \end{cases} \tag{28}$$

where $t_{u,1}$ and $t_{u,2}$ are the times of initial and reversal points for $\triangle\sigma_{u,HSS}$, respectively; which could be identified during the rainflow counting process (see Fig. 3).

Meanwhile, the derivative of HSS $\frac{d\sigma_{u,HSS}}{d\mathbf{b}}$ was determined from

$$\frac{d\sigma_{u,HSS}}{d\mathbf{b}} = c_{Nx}\left(\frac{dSCF_{Nx}}{d\mathbf{b}}\sigma_{u,Nx} + SCF_{Nx}\frac{d\sigma_{u,Nx}}{d\mathbf{b}}\right) + c_{My}\left(\frac{dSCF_{My}}{d\mathbf{b}}\sigma_{u,My} + SCF_{My}\frac{d\sigma_{u,My}}{d\mathbf{b}}\right) + c_{Mz}\left(\frac{dSCF_{Mz}}{d\mathbf{b}}\sigma_{u,Mz} + SCF_{Mz}\frac{d\sigma_{u,Mz}}{d\mathbf{b}}\right). \tag{29}$$

The constants c_{Nx}, c_{My} and c_{Mz} may change depending on the HSS locations [24]. Since the SCFs are generally governed by the joint dimensions, the derivatives $\frac{dSCF}{d\mathbf{b}}$ can be calculated using the direct differentiation method as well. As for the nominal stresses $\sigma_{u,Nx}$, $\sigma_{u,My}$ and $\sigma_{u,Mz}$, the derivatives could be evaluated using the same method as explained for the extreme load constraints.

Lastly, the gradient of eigenfrequencies ∇g_3 was computed using

$$\nabla g_3 = \frac{1}{4\pi}\lambda_l^{-\frac{1}{2}}\frac{\partial\lambda_l}{\partial\mathbf{b}} \tag{30}$$

$$\text{and } \frac{\partial\lambda_l}{\partial\mathbf{b}} = \phi_l^T\left(\frac{\partial[\mathbf{K}]}{\partial\mathbf{b}} - \lambda_l\frac{\partial[\mathbf{M}]}{\partial\mathbf{b}}\right)\phi_l \tag{31}$$

where λ_l is the eigenvalue of lth mode; and ϕ_l is the eigenvector of lth mode, as derived in Ref. [31].

3.5. Optimization algorithm

The constrained NLP problem was approximated and solved using the Sequential Quadratic Programming (SQP) approach at each iteration. The integrated code implemented the SQP subroutine available from the Matlab optimization toolbox [32]. The SQP algorithm reformulates the general problem as a QP subproblem and approximates the Hessian matrix (second-order derivative of the Lagrange function) using the modified Broyden-Fletcher-Goldfarb-Shanno (BFGS) formula. This guarantees positive definite Hessian matrices and ensures that the subproblems are strictly convex. More details about the SQP method can be found in Ref. [33].

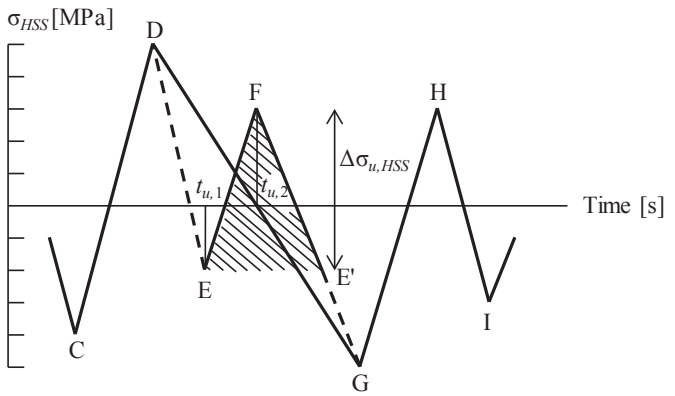

Fig. 3. Rainflow counting process. In this example, E-F-E′ is counted as one full stress cycle, where $\triangle\sigma_{u,HSS}$ is the uth HSS range, $t_{u,1}$ and $t_{u,2}$ are the corresponding time steps at E (initial point) and F (reversal point), respectively.

4. A case study on offshore wind turbine jacket substructures

As a case study, the integrated code was implemented on the numerical wind turbine system used within the IEA Task 30 OC4 Phase I Project. The system is formed by the NREL 5-MW horizontal axis three-bladed baseline turbine mounted on top of the support structure system that consists of a monopile tower, a transition piece and a jacket substructure. The overall finite element model is shown in Fig. 2(a). The reference wind turbine model was discretized into customized beam elements following the distributed blade structural properties in Ref. [34]. The overall elevation on which the RNA is installed was modified according to [35]. As for the monopile tower, it was represented using 18 segments of Euler-Bernoulli beam elements with different cross-sectional areas. The transition piece that is supposed to be a rigid concrete block, was modeled using a lumped mass system which gives the same mass and inertia distributions in X-, Y- and Z-directions as the actual model. The Young's modulus of beam elements within the lumped mass model was adjusted to 10^4-fold the actual value to generate high rigidity. Pile members below the seabed were not included in the study and the turbine was assumed to be fixed at the ground. Rayleigh damping was used to model structural damping for the support structure. A critical damping ratio of 1 percent was assumed for the first and second eigenmodes of the support structures, which includes the tower, transition piece and jacket substructure.

When generating rotor loads, the same finite element model was built for the RNA in FEDEM Windpower, while being fixed at the yaw node. A generator-torque controller and a rotor-collective blade-pitch controller were implemented to regulate the rotor rotational speed, in accordance with [34]. As for the aerodynamic modeling, the generalized dynamic wake model was utilized without considering the tower influence.

4.1. Design variables

The interest of this study is to optimize the dimensions of the jacket substructure. Two different jacket models were evaluated: the OC4 and the UpWind jackets [35,36]. The former is a simplified model adapted from the latter that comprises joint cans for reinforced structural performance around the tubular joints. The joint cans were modeled explicitly for the UpWind model by introducing more design variables, which can be modified independently from the tubular members. A total number of 22 and 38 design variables were defined for each model as indicated in Fig. 4(a) and (b). The odd and even indexed variables denote the member outer diameters and thicknesses, respectively, i.e. $[b_1, b_2, b_3, b_4, \ldots, b_{M-1}, b_M] = [D_1, T_1, D_2, T_2, \ldots, D_{M/2}, T_{M/2}]$. The tubular members were represented using Euler-Bernoulli beam elements whereas the tubular joints were modeled as members connected rigidly at the intersection points of the members' centerlines, i.e. the overlap in members and the local joint flexibility (LJF) at the tubular joints were not accounted

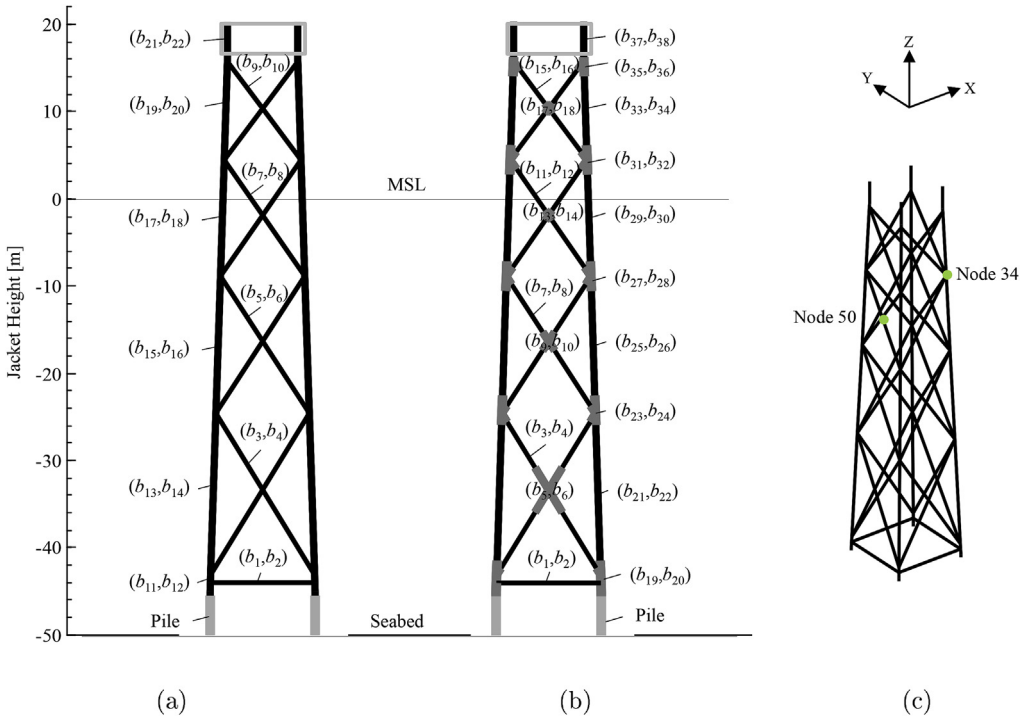

Fig. 4. Design variables defined for (a) the OC4 jacket and (b) the UpWind jacket. (c) Output locations node 34 (K-joint) and node 50 (X-joint).

for in this study. The legs of the jacket were assumed to be free flooded by seawater while the braces were not. The substructure between water depths of −2 m and −40 m was covered with a layer of marine growth that has a thickness of 0.1 m and a density of 1100 kg/m^3, following the [35].

The material properties of the steel jacket are summarized in Table 1. Bilinear S-N curves were used in the fatigue analysis. All components above the MSL referred to the S-N curves in air whereas the submerged parts used the S-N curves in seawater with cathodic protection [24].

Five sets of initial dimensions $\mathbf{b}^{(0)}$ were investigated on the OC4 jacket (initial designs 1–5) and one set for the UpWind jacket (initial design 1). The initial design 1 refers to the original OC4 jacket dimensions, while others are randomly generated. The lower and upper bounds $\mathbf{b}_{min}$ and $\mathbf{b}_{max}$ were set to 30 percent and 300 percent of the OC4 jacket dimensions, respectively. Fig. 5 explains the geometrical terms for tubular joints as defined in this study, while Table 2 summarizes the validity range of various sizing dimensions with reference to the limit state functions implemented. For D_{chord}/T_{chord} and D_{can}/T_{can}, a smaller bound between 20 and 64 was used instead, upon combining the recommendations from both standards.

4.2. Design load cases

The OWT model was subjected to combined wind-wave loads. The DLCs were established based on the UpWind design basis for a deep-water site. The wind and wave data was gathered from a 3-h average for a period of 22 years at the K13 platform in the Dutch North Sea [37]. Tables 3 and 4 summarize the extreme and fatigue DLCs used in the optimization simulations. They correspond to the partial load cases carried out for the final design phase in the UpWind project [36]. The wind condition was modeled as a three-dimensional turbulent wind field according to the Kaimal spectrum, while the wave condition was modeled as a Wheeler stretched irregular wave following the JONSWAP spectrum based on the linear wave theory. The wind field parameters include hub height wind speeds V_w, turbulent intensities TI, wind gradient exponents α, while the wave field parameters consist of significant wave heights H_s, peak spectral periods T_p and peak shape parameters γ.

The DLC 6.1a simulated extreme winds and waves with a 50-year returning period where the OWT was modeled in idling mode. Regarding the FLS DLCs, both DLCs 1.2 and 6.4 were combined into a reduced (lumped) scatter diagram that segregates the events based on different V_w bins and event probabilities P_v. The DLC 1.2 modeled the turbine in power production mode that operates in the normal turbulent wind and wave conditions; whereas the DLC 6.4 modeled the turbine to be idling under the wind conditions below the cut-in and above the cut-out wind speeds. All turbine blades at idling were feathered to the pitch angle of 90° to neutralize the torque on the rotor shaft, without applying a brake. Both winds and waves were assumed to be co-directional and applied in the global X-direction towards the side of the jacket where the turbine was facing to without any yaw error (see Fig. 2(a)). Besides, no current model was included in the simulations. For each DLC, a dynamic analysis with a simulation period of 660 s was carried out. The first 60 s of the simulation results were discarded to allow initial transients to decay. This has been abbreviated from the simulation time recommended by the IEC standard or the offshore recommended practice, in order to shorten the computational time required for the case study. Furthermore, a time step of 0.025 s was used to generate the rotor load time series in FEDEM Windpower and also for the numerical integration in the Matlab dynamic solver. During the optimization process, the same sets of turbulent wind seeds and irregular wave seeds were retained for all iterations.

5. Results and discussion

5.1. Accuracy of dynamic analysis

Fig. 6 depicts an exemplary result of the response power spectral densities (PSD) obtained at node 50 (see Fig. 4(c)) by using different dynamic solvers. Results show that the in-house dynamic solver exhibited good agreements with FEDEM Windpower, not only in identifying the critical excitation and global eigenfrequencies, but also in matching the spectral

Table 1
Material properties of steel used for the jacket substructure.

Parameter	Notation [units]	Numerical values
Density	ρ_s [kg/m^3]	7.8E+3
Young's modulus	E_s [Pa]	2.1E+11
Yield strength	f_{ys}[Pa]	2.6E+8
Poisson's ratio	ν	0.3
S-N curve 1 in air ($N \leq 10^7$ cycles)	m_1	3.0
	$\log \bar{a}_1$	12.164
S-N curve 2 in air ($N > 10^7$ cycles)	m_2	5.0
	$\log \bar{a}_2$	15.606
S-N curve 1 in seawater ($N \leq 10^6$ cycles)	m_1	3.0
	$\log \bar{a}_1$	11.764
S-N curve 2 in seawater ($N > 10^6$ cycles)	m_2	5.0
	$\log \bar{a}_2$	15.606

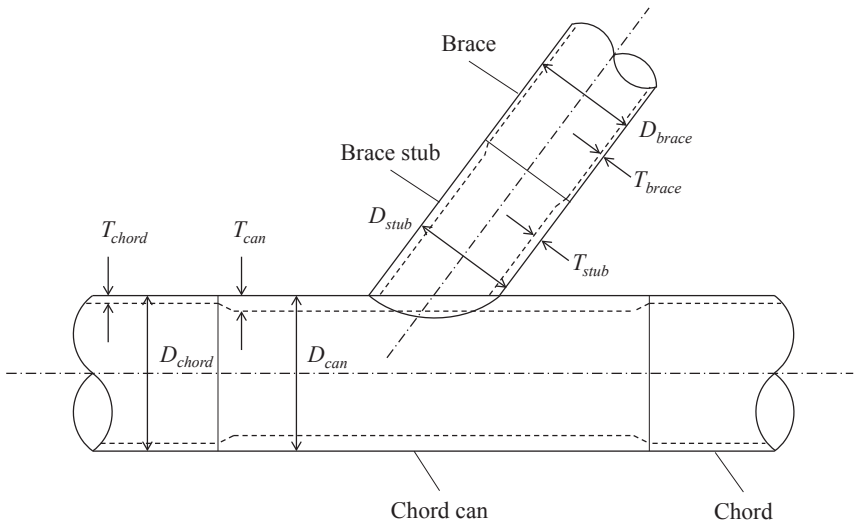

Fig. 5. Geometrical definitions of tubular joints.

Table 2
Validity range of various sizing dimensions for a tubular joint.

Variables	Lower bound	Upper bound	Reference
D_{stub}/D_{can}	0.2	1.0	[22,24]
T_{stub}/T_{can}	0.2	1.0	[24]
T_{can}/T_{chord} and T_{stub}/T_{brace}	–	2.0	[24]
D_{chord}/T_{chord} and D_{can}/T_{can}	16	64	[24]
	20	100	[22]
D_n/T_n	–	120	[22]

Table 3
Extreme design load case.

DLC	V_w [m/s]	TI [%]	α [–]	H_s [m]	γ [–]	T_p [s]
6.1a	42.73	11.0	0.11	9.40	3.3	13.70

Table 4
Fatigue design load cases.

DLC	V_w [m/s]	TI [%]	α [–]	H_s [m]	T_p [s]	γ [–]	P_v [%]
6.4a	2.0	29.2	0.14	1.07	6.03	1.0	4.958
1.2a	4.0	20.4	0.14	1.10	5.88	1.0	9.985
1.2b	6.0	17.5	0.14	1.18	5.76	1.0	11.333
1.2c	8.0	16.0	0.14	1.31	5.67	1.0	13.491
1.2d	10.0	15.2	0.14	1.48	5.74	1.0	12.287
1.2e	12.0	14.6	0.14	1.70	5.88	1.0	12.982
1.2f	14.0	14.2	0.14	1.91	6.07	1.0	9.995
1.2g	16.0	13.9	0.14	2.19	6.37	1.0	8.729
1.2h	18.0	13.6	0.14	2.47	6.71	1.0	5.723
1.2i	20.0	13.4	0.14	2.76	6.99	1.0	3.836
1.2j	22.0	13.3	0.14	3.09	7.40	1.0	3.304
1.2k	24.0	13.1	0.14	3.42	7.80	1.0	1.489
6.4b	30.0	11.8	0.14	4.46	8.86	1.0	1.701

power contents. The fully coupled aero-hydro-servo-elastic simulations carried out in FEDEM Windpower give the most accurate response analysis, since the coupling effects and non-linearities are accounted for. At low frequencies between 0.1 and 1.0 Hz, the inconspicuous differences between the codes could be due to different finite element models adopted instead of the coupling and aerodynamic non-linearities, as suggested by the excellent agreement between the coupled and decoupled simulations in FEDEM Windpower. FEDEM Windpower implements the Euler-Bernoulli beam theory with

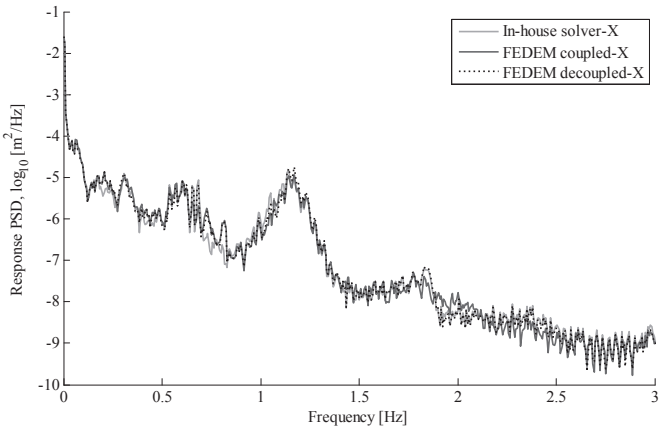

Fig. 6. Dynamic response PSD of node 50 (X-joint) in global X-direction under DLC 1.2e.

quadratic shape functions, whereas classical 3rd order shape functions are used for the in-house code. Besides, fatigue damage estimations correlate strongly with the dynamic response PSD as it is used in the spectral FLS approach. Therefore, the result gives good indications that the fatigue analysis can be carried out reliably using the linear decoupled method. The method works well for bottom fixed substructures that are relatively rigid, as they exhibit little nonlinear characteristics. However, care must be taken when applying to the method for softer support structures, such as compliant towers.

Fig. 7 depicts the probability density functions (PDF) of structural responses obtained at node 34 (see Fig. 4(c)) under DLC 6.1a. In general, slight deviations were observed among the PDF, with the in-house solver yielding the widest distributions in most DOFs, followed by the FEDEM decoupled model. These differences can be explained in part by the fact that the in-house solver considers both aerodynamic damping and hydrodynamic damping to be linear, while the FEDEM decoupled model uses only the former. When subjected to severe wind and wave loads, the non-linearities within aerodynamic and hydrodynamic drag forces become prominent, thus generating larger dampening effects. As for the aerodynamic damping, it is usually relatively small for the extreme load case DLC 6.1a, since the turbine is idling. Nevertheless, the deviations are deemed acceptable for the in-house code, as a larger spread of response tends to generate more conservative results in the extreme load analysis.

In addition, the load simulations of OWT jacket substructures can be sensitive to the joint modeling techniques. In this study, LJF was omitted for simplification purposes. More realistic representation of tubular joints using the advanced superelement method for instance can attain a higher level of accuracy when studying the global and local dynamics of the structures, and therefore can have impacts on the load distribution path and the fatigue analysis of the tubular joints [38].

5.2. Performance of integrated optimization method

The optimization of the OC4 jacket model was carried out by applying the proposed analytical method and the conventional finite difference approach for the design sensitivity analysis. Fig. 8 displays the variations of objective functions and maximum constraint violations during the optimization process. It is apparent from this figure that the analytical gradient-based method was more efficient than the finite difference approach in searching for the optimal design, as fewer iterations were required to attain the convergence of solutions. The findings are consistent with previous research, which found that the finite difference sensitivity information could be unreliable and inaccurate when applied in the offshore wind dynamic

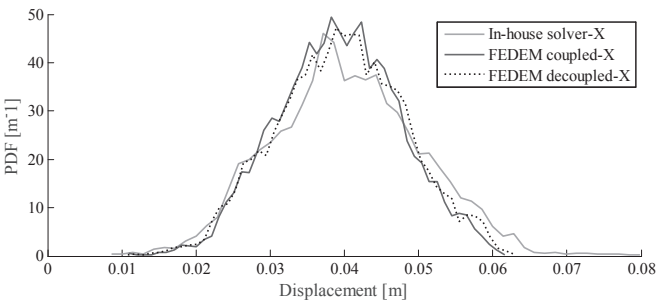

Fig. 7. Dynamic response PDF of node 34 (K-joint) in global X-direction under DLC 6.1a.

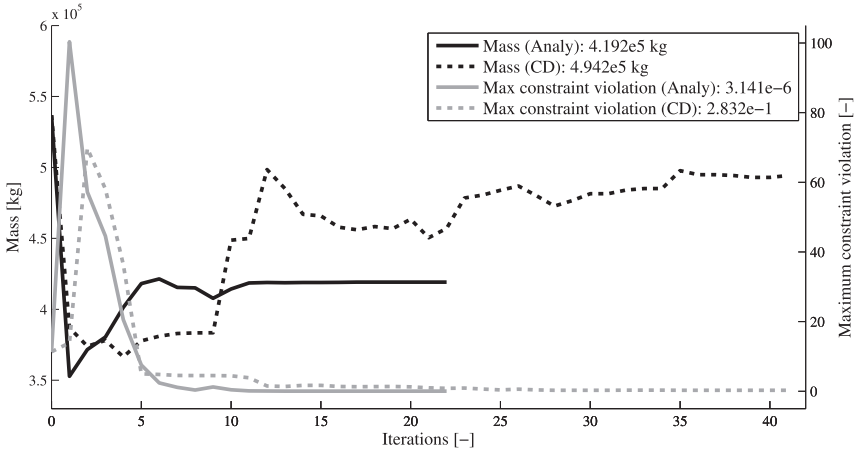

Fig. 8. Variation of design objective functions and maximum constraint violations during the optimization of the OC4 jacket substructure (initial design 1). The numbers in the legend refer to the corresponding values at the final iteration. Analy: analytical method. CD: central difference method.

problem, and therefore resulting in slow convergence. Moreover, the improved efficiency also extends to the computation at each iteration, since only $M + 1$ number of system analyses are required, as compared with $2M + 1$ for the central difference (CD) method, for every function and gradient evaluation, where M is the number of design variables. Additionally, the analytical gradient-based method can recycle the [**M**], [**C**] and [**K**] matrices as well as the eigenvectors (eigenvalues) solved in Eq. (18) for the gradient evaluations in Eq. (26). This saves the computational time required for assembling the finite element models and solving the eigenvalue problems. The number of iterations taken for the analytical gradient-based method to converge varied moderately among the 5 initial designs tested, ranging between 22 and 31 iterations.

Another important observation made is that the accuracy of the optimization procedure was affected, since the finite difference gradient-based method converged to a different solution which was heavier and infeasible. Figs. 9 and 10 show the dimensions and performance of the initial and optimized jacket designs presented in the study. In general, the diameter-to-thickness ratios of legs and braces were smaller for the optimal design given by the analytical gradient-based approach. Both optimal designs have shown improvements in diminishing the constraint violations occurring at the X-braces. However, being misled by the incorrect approximation of constraint gradients, the thicknesses of leg members were reduced too much to maintain the required buckling strengths at the central bays. As the OWT system is exposed to high cycle fatigue loads, the accuracy of finite difference approximations can be susceptible to the step sizes used in perturbing the design variables, the time steps applied in the numerical integration, the joint or HSS locations where the gradients are evaluated, etc. [20]. Besides, for tubular beams that experience alternating tension-compression modes, numerical artifacts can occur when calculating the extreme load constraint sensitivities, due to the possible mismatches of ULS values at the affected time steps [19]. As some of these factors can be interdependent, it would be very computationally taxing to determine the “optimal” values to use, especially when a large number of design load constraints are implemented.

It is also interesting to note that the mathematical formulae for the sensitivity analysis, i.e. Eqs. 22–31 can be generalized to include variations with respect to member lengths, brace angles and leg distances. This allows for studying more general changes in the configuration of OWT jacket substructures during optimization. However, the needed sensitivity derivatives will be more complicated to calculate, and it is presently unclear if the gradient-based optimization algorithm will be effective in solving such more general configuration optimal design problems.

5.3. Local and global optimal solutions

In Figs. 9 and 10, all the initial designs 1–5 converged to the same optimal OC4 jacket solution using the analytical gradient-based method. The first-order optimality, i.e. a necessary but not sufficient measurement of the solution being at minimum, fell below the bound of 10^{-6}; while the maximum constraint violation was less than the constraint tolerance of 10^{-4}, for all cases. For this design problem, the local uniqueness of solution is guaranteed since the external loads, initial conditions and boundary conditions applied do not vary independently with respect to the design variables during the iterations. A check on the nearby points of the solution or a multi-start analysis as performed did not find any better solution, thus strongly indicating that an optimum is found. However, as the overall problem formulation is non-convex, the proposed gradient-based algorithm may only locate a local optimum instead of the global optimum during the optimization process. Multiple repetitions of the same local optimization procedures were carried out from different starting points, in an attempt to search in more than one possible basin of attraction. Interestingly, it seems possible that the large number of design constraints formulated in the problem has constrained the feasible regions significantly enough for the global optima to be attained in this sizing optimization problem. Although it is not the main interest of this study to prove the convexity of the

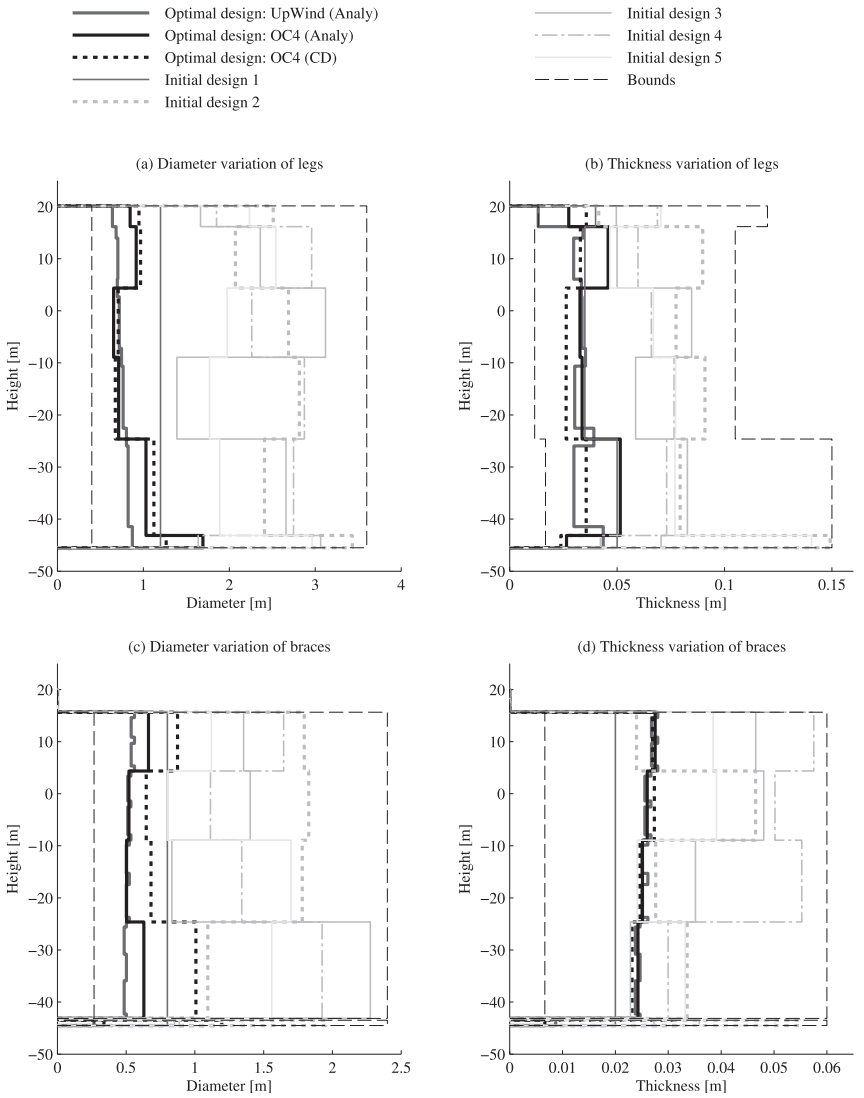

Fig. 9. Dimensions of initial and optimized designs for the jacket substructures. Analy: analytical method. CD: central difference method.

design optimization problem, it can be observed that the mass reduction objective function which is a hyperbolic paraboloid (non-convex), for instance, has become convex within the sizing constraints implemented. Nevertheless, it is still very challenging to determine the situation for the dynamic load constraints. All the starting points used in the study were sampled from the design space that fulfills the sizing constraints (but not the load constraints); while the SQP algorithm applied strictly obeys the bounds at every iteration.

5.4. Influence of design constraints on structural design and optimization process

The influence of design constraints on the structural design and behavior is quite revealing in several ways. Comparing Figs. 9 and 10, it can be seen that the mass reduction attained in the optimized design depends strongly on how well each structural component is utilized against the prescribed limit state functions. The trade-offs among the leg and brace dimensions to maximize the utilization are non-trivial and complex. Competition exists among the design constraints to be the critical design factor, while the criticality can change during the course of optimization. For instance, in the UpWind jacket configuration, the buckling load constraints on the leg members overtook the fatigue load constraints at the TYK-joints (leg side) to be the critical constraints for the topmost leg section. As for the braces, the X-joints are normally more critical than the TYK-joints, since higher SCFs are produced around the X-joints. Furthermore, being higher in fidelity, the UpWind jacket allowed better utilization of structural strengths for the members and joints. As a result, it yielded an optimal design that was 22 percent lighter in comparison with the OC4 counterpart. The inclusion of joint cans in the design modeling spread

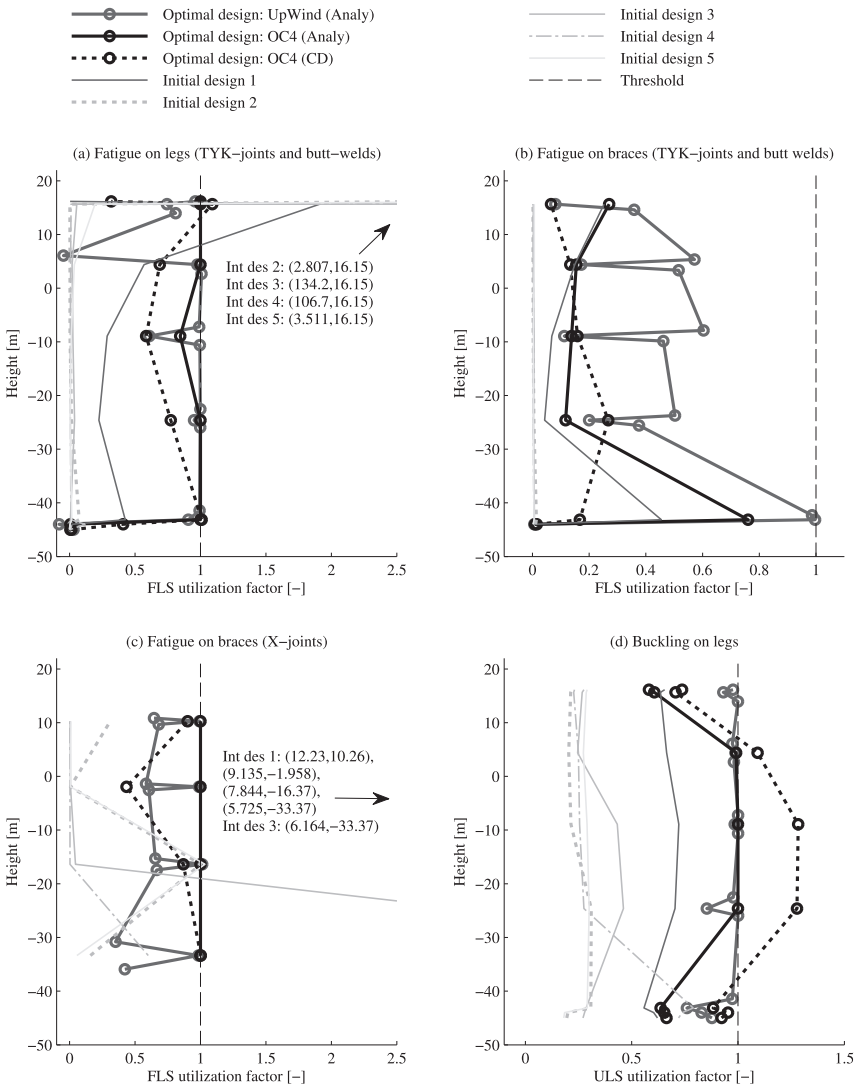

Fig. 10. Structural performance of initial and optimized designs for the jacket substructures. The coordinates (x-utilization factor, y-height) of several points that are outside the plot limits are labeled in (a) and (c). Analy: analytical method. CD: central difference method.

the geometry of legs and braces more evenly, where the outer diameters of legs were decreasing gradually from bottom to top, while the thicknesses of braces were following the opposite.

Besides, a more realistic optimal design would require more load cases and longer simulation times when formulating the design constraints. In fact, hundreds and thousands of load simulations considering different DLCs and loading directions ought to be carried out, while each simulation should run at least 1 h according to IEC standard or at least 3 h for wave loads according to the recommended practice in offshore engineering. Nevertheless, by incorporating the critical DLCs in the opitmization process as attempted here, the integrated methodology can be used to generate preliminary designs that are lighter and better utilized. The use of shorter simulations is generally sufficient for optimization purposes, since it is more important to obtain accurate estimates of the changes in the design constraint than of the actual design constraint itself. For jackets substructures, it was also found that wind loads contribute most to the uncertainty in the fatigue lifetime estimate compared to wave loads, and therefore it seems not necessary to use full 3 h simulations for the dynamic analysis [39]. Of course the final, converged design needs to be verified and fine-tuned with further analysis and longer simulation runs in the detailed design stage.

On the other hand, Figs. 11 and 12 display the variations of eigenfrequency, extreme load and fatigue load constraints during the optimization process. The first mode side-to-side and fore-aft eigenfrequencies varied in a similar pattern as the structural mass, implying that a lighter support structure correlates to 'softer' design. The eigenfrequencies fluctuated within the allowable limits and finally converged to approximately 0.28 Hz. This finding is somehow different from the case study of a monopile tower which was investigated in Refs. [18], whereby the first mode eigenfrequency converged to the $1P_U$. The

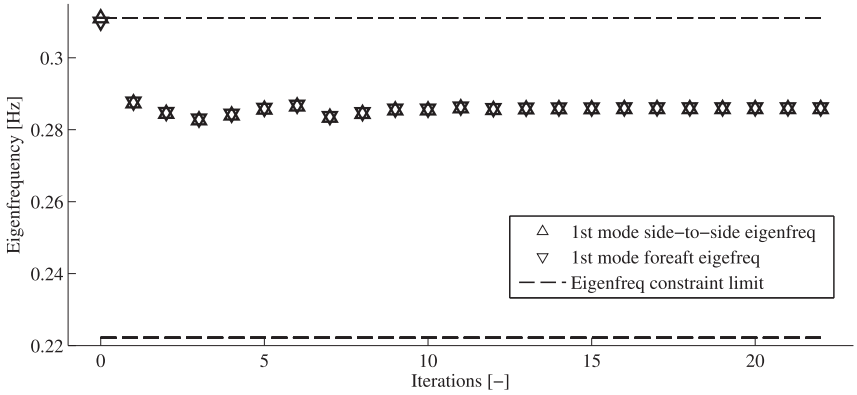

Fig. 11. Variation of eigen frequency constraint functions during the optimization of the OC4 jacket substructure (initial design 1).

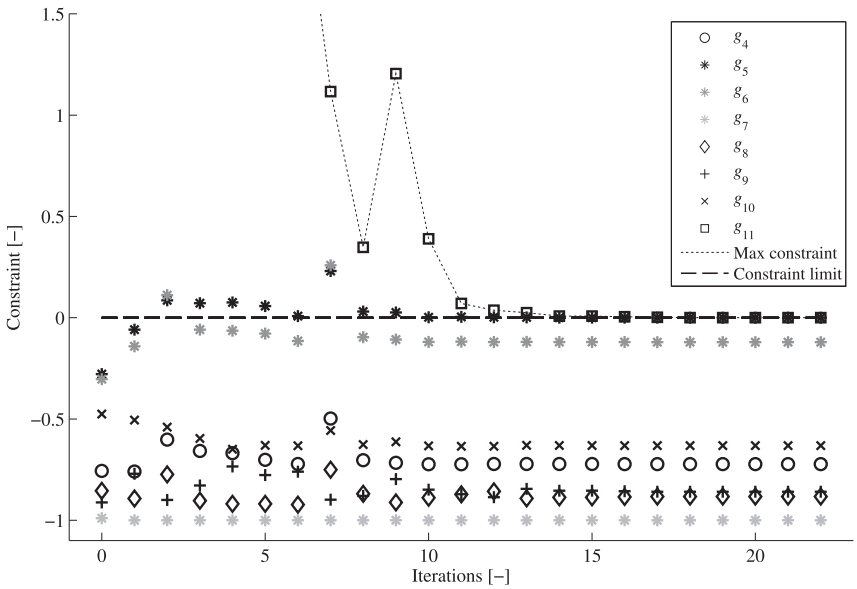

Fig. 12. Variation of extreme and fatigue load constraint functions during the optimization of the OC4 jacket substructure (initial design 1).

jacket substructures are generally stiffer than the monopile towers, therefore do not allow significant dips in the eigenfrequencies, particularly when only sizing optimization is considered. In addition, multiple eigenfrequency checks can be included in the optimization design studies to avoid local vibrations at the overhanging X-braces, for instance, which can occur at high excitation frequencies, i.e. multiples of blade passing frequencies. Among all the design load constraints, the buckling and compressive load constraint g_5 and g_6, as well as the fatigue load constraint g_{11} were found active during the optimization process (see Fig. 12). The tensile state function g_4 and extreme load constraint for tubular joints g_{10} were relatively more active in fluctuating within the allowable limit. In contrast, the variation of g_8 and g_9 were very small at all iterations. Long tubular members generally experience minimal shear force and torsional moment in frames whereby the diameters of members are also relatively too small for hoop buckling to occur. Moreover, g_7 is a conditional design constraint, and it was not activate in most of the iterations. As highlighted previously, g_5 and g_{11} remained as the active constraints until the final iterations, where g_5 tended to gain influence when the design was gradually tuned to be less fatigue prone towards the end. Nevertheless, g_{11} is generally the final design constraint to converge during the optimization of the OC4 jacket substructure.

Importantly, the result signifies that both design constraints should be included concurrently in the optimization procedure, instead of handling them sequentially. Although infeasible, the “optimized” solution produced by the CD gradient-based method shows that the buckling failure mode could be possibly more prominent than the fatigue failure mode for offshore wind turbine frame structures, which goes against the general belief within the industry that the structures should be fatigue driven.

6. Conclusions

This paper has presented an analytical gradient-based optimization framework for the design of OWT support structures. The method implemented a comprehensive scope of design checks on sizing, eigenfrequencies, extreme load and fatigue load analyses as the design constraints, while minimizing the overall structural mass. The design sensitivities were calculated analytically using the DDM. A case study that was set to evaluate the performance of the proposed method revealed that:

1. The in-house dynamic solver which assumed a combined linear hydro-elastic model with decoupled aero-servo loads has demonstrated reliable and conservative response analyses against the fully coupled non-linear simulations carried out using the commercial code FEDEM Windpower.
2. The framework was capable of delivering higher efficiency and accuracy in the optimization process compared to the conventional finite difference gradient-based method, thanks to the analytical sensitivity derivatives. A considerable amount of computational time can be saved in the optimization iterations, the calculation of gradients, the matrix assembly and solving the eigenvalue problems. Besides, the functionality of the framework was shown to be robust against the change of starting points.
3. The converged solution obtained in the design optimization study of the OC4 jacket was probably the global optimum, as inferred by the exact convergence of all design solutions in the multi-start analysis. Interestingly, the highly constrained problem formulation adopted seems to have restricted the feasible zones significantly for the global optimum to be found easily in this non-convex problem.
4. The optimal solution in the structural design problem is closely related to how well the individual components can be utilized against the prescribed limit state functions, but this is muddled by the trade-offs among the components to maximize the utilization and the competition between the design constraints which is to be the critical design driver. Among all design constraints applied, the buckling and fatigue load constraints on TYK-joint were the design drivers for legs, whereas the fatigue load constraints on X-joints had high influence on the design of braces.

Acknowledgments

The help of Sebastian Schafhirt from Department of Civil and Transport Engineering, Norwegian University of Science and Technology in providing the aerodynamic damping data and facilitating the simulations in NTNU is highly appreciated. Support from the Singapore Economic Development Board (EDB) – DNV GL – Energy Research Institute @ NTU (ERI@N) Joint Industry Ph.D. Program and the Norwegian Research Centre for Offshore Wind Technology (NOWITECH FME, project no. 193823) is gratefully acknowledged.

References

[1] Esteban MD, Diez JJ, López JS, Negro V. Why offshore wind energy? Renew Energy 2011;36(2):444–50. http://dx.doi.org/10.1016/j.renene.2010.07.009. URL.
[2] WEC. World energy perspective – cost of energy technologies. World Energy Council, Rept. London. 2013. URL, http://www.worldenergy.org/wp-content/uploads/2013/09/WEC_J1143_CostofTECHNOLOGIES_021013_WEB_Final.pdf.
[3] Consulting Navigant. Offshore wind market and economic analysis - annual market assessment. Navigant Consulting, Rept DE-EE0005360. Burlington, MA. 2013. URL, http://www1.eere.energy.gov/wind/pdfs/offshore_wind_market_and_economic_analysis_10_2013.pdf.
[4] The Crown Estate. Offshore wind cost reduction – Pathways study. The Crown Estate, Rept. London. 2012.
[5] Willows C, Valpy B. Approaches to cost-reduction in offshore wind. BVG Associates. Wiltshire. 2015. URL, https://www.theccc.org.uk/wp-content/uploads/2015/06/BVG-Associates-2015-Approaches-to-cost-reduction-in-offshore-wind.pdf.
[6] Vorpahl F, Schwarze H, Fischer T, Seidel M, Jonkman J. Offshore wind turbine environment, loads, simulation, and design. Wiley Interdiscip Rev Energy Environ 2013;2(5):548–70. URL, http://doi.wiley.com/10.1002/wene.52.
[7] IEC. Wind turbines - Part 3: design requirements for offshore wind turbines. International Electrotechnical Commission, International Standard IEC 61400-3. Geneva. 2009.
[8] Uys P, Farkas J, Jármai K, van Tonder F. Optimisation of a steel tower for a wind turbine structure. Eng Struct 2007;29(7):1337–42. http://dx.doi.org/10.1016/j.engstruct.2006.08.011. URL, http://linkinghub.elsevier.com/retrieve/pii/S0141029606003464.
[9] Kang BS, Park GJ, Arora JS. A review of optimization of structures subjected to transient loads. Struct Multidiscip Optim 2006;31(2):81–95. http://dx.doi.org/10.1007/s00158-005-0575-4. URL, http://link.springer.com/10.1007/s00158-005-0575-4.
[10] Karadeniz H, Togan V, Vrouwenvelder T. An integrated reliability-based design optimization of offshore towers. Reliab Eng Syst Saf 2009;94(10):1510–6. http://dx.doi.org/10.1016/j.ress.2009.02.008. URL, http://linkinghub.elsevier.com/retrieve/pii/S0951832009000593.
[11] Yang H, Zhu Y. Robust design optimization of supporting structure of offshore wind turbine. J Mar Sci Technol 2015;20(4):689–702. http://dx.doi.org/10.1007/s00773-015-0323-4. URL, http://link.springer.com/10.1007/s00773-015-0323-4.
[12] Muskulus M, Schafhirt S. Design optimization of wind turbine support structures - a review. J Ocean Wind Energy 2014;1(1):12–22. URL, http://www.isope.org/publications/jowe/jowe-01-1/JOWE-01-1-p012-jcr10-Muskulus.pdf.
[13] Chew KH, Ng EYK, Tai K, Muskulus M, Zwick D. Offshore wind turbine jacket substructure: a comparison study between four-legged and three-legged designs. J Ocean Wind Energy 2014;1(2):74–81. URL, http://www.isope.org/publications/jowe/jowe-01-2/JOWE-01-2-p074-jcr09-Chew.pdf.
[14] Long H, Moe G. Preliminary design of bottom-fixed lattice offshore Wind turbine towers in the fatigue limit state by the frequency domain method. J Offshore Mech Arct Eng 2012;134(3):031902. http://dx.doi.org/10.1115/1.4005200. URL, http://offshoremechanics.asmedigitalcollection.asme.org/article.aspx?articleid=1457850.
[15] Yoshida S. Wind turbine tower optimization method using a genetic algorithm. Wind Eng 2006;30(6):453–69. http://dx.doi.org/10.1260/030952406779994150. URL, http://multi-science.metapress.com/openurl.asp?.
[16] Schafhirt S, Zwick D, Muskulus M. Reanalysis of jacket support structure for computer-aided optimization of offshore wind turbines with a genetic algorithm. J Ocean Wind Energy 2014;1(4):209–16. URL, http://www.isope.org/publications/jowe/jowe-01-4/JOWE-01-4-p209-tsr02-Schafhirt.pdf.

[17] Ashuri T, Zaaijer M, Martins J, van Bussel G, van Kuik G. Multidisciplinary design optimization of offshore wind turbines for minimum levelized cost of energy. Renew Energy 2014;68:893–905. http://dx.doi.org/10.1016/j.renene.2014.02.045. URL, http://www.sciencedirect.com/science/article/pii/S0960148114001360.
[18] Haghi R, Ashuri T, Valk PLCVD, David P. Integrated multidisciplinary constrained optimization of offshore support structures. J Phys Conf Ser 2014; 555(012046):1–10. http://dx.doi.org/10.1088/1742-6596/555/1/012046.
[19] Chew KH, Tai K, Ng EYK, Muskulus M. Optimization of offshore wind turbine support structures using an analytical gradient-based method. Energy Procedia 2015;80(December):100–7. http://dx.doi.org/10.1016/j.egypro.2015.11.412. URL, http://linkinghub.elsevier.com/retrieve/pii/S187661021502144X.
[20] Chew KH, Muskulus M, Srikanth N, Tai K, Ng EYK. Fatigue sensitivity analysis of offshore wind turbine structures. In: Proc WCSMO-11. Sydney, Australia; 2015. http://dx.doi.org/10.13140/RG.2.1.4757.3849. 1339:1–6. URL, http://www.aeromech.usyd.edu.au/WCSMO2015/papers/1339_paper.pdf.
[21] DNV. Design of offshore steel structures, general (LRFD method). Det Norske Veritas, Offshore Standard DNV-OS-C101. Høvik. 2011.
[22] Standards Norway. Design of steel structures. NORSOK Standard N-004. Lysaker, Norway. 2013.
[23] Van der Tempel J, Molenaar DP. Wind turbine structural dynamics - a review of the principles for modern power generation, onshore and offshore. Wind Eng 2002;26(4):211–20.
[24] DNV. Fatigue design of offshore steel structures. Det Norske Veritas, Recommended Practice DNV- RP-C203. Høvik. 2012.
[25] ASTM. Standard practices for cycle counting in fatigue analysis. American Society for Testing and Materials, ASTM E1049–85. West Conshohocken, PA. 2011. http://dx.doi.org/10.1520/E1049-85R11E01.2.
[26] Fedem Technology AS. Fedem Windpower user's guide release 7.1. Trondheim. 2014.
[27] Laino DJ, Hansen AC. User's guide to the wind turbine dynamics aerodynamics computer software AeroDyn. Windward Engineering, Tech Rept. Salt Lake City, UT. 2002.
[28] Jonkman BJ. TurbSim user's guide: Version 1.50. National Renewable Energy Laboratory, Tech Rept NREL/TP 46198. Golden, CO. 2009.
[29] Salzmann D, Van Der Tempel J. Aerodynamic damping in the design of support structures for offshore wind turbines. In: Proc Copenhagen offshore Conf. Copenhagen, Denmark; 2005. p. 9.
[30] Park GJ. Analytic methods for design practice. London: Springer; 2007. http://dx.doi.org/10.1007/978-1-84628-473-1. ISBN 978-1-84628-472-4. URL, http://link.springer.com/10.1007/978-1-84628-473-1.
[31] Fox RL, Kapoor MP. Rates of change of eigenvalues and eigenvectors. AIAA J 1968;6(12):2426–9. http://dx.doi.org/10.2514/3.5008. URL, http://arc.aiaa.org/doi/abs/10.2514/3.5008.
[32] MathWorks Inc. Optimization toolbox for use with MATLAB R2014: user's guide. ver 7.0 ed. Natick, MA: MathWorks Inc; 2014.
[33] Arora JS. Introduction to optimum design. 3rd ed. Oxford: Academic Press; 2011.
[34] Jonkman J, Butterfield S, Musial W, Scott G. Definition of a 5-MW reference wind turbine for offshore system development. National Renewable Energy Laboratory, Tech Rept NREL/TP-500-38060. Golden, CO. 2009.
[35] Vorpahl F, Popko W, Kaufer D. Description of a basic model of the "UpWind reference jacket" for code comparison in the OC4 project under IEA Wind Annex 30. Franhofer IWES, Tech Rept. Bremerhaven. 2011.
[36] Vemula NK. Design solution for the Upwind reference offshore support structure. Rambøll, Tech Rept UpWind WP4 D4.2.5. Esbjerg. 2010.
[37] Fischer T, de Vries W, Schmidt B. Upwind design basis (WP4: offshore foundations and support structures)U. niversität Stuttgart, Tech Rept UpWind WP4. Stuttgart. 2010.
[38] Tu Y, Vorpahl F. Influence of superelement support structure modeling on the loads on an offshore wind turbine with a jacket support structure. J Ocean Wind Energy 2014;1(3):153–60. URL, http://www.isope.org/publications/jowe/jowe-01-3/01-3-p153-jc-r-11-Tu.pdf.
[39] Zwick D, Muskulus M. The simulation error caused by input loading variability in offshore wind turbine structural analysis. Wind Energy 2015;18(8): 1421–32. URL, http://doi.wiley.com/10.1002/we.1767.